



Research

Cite this article: Brely L, Bosia F, Pugno NM. 2015 Numerical implementation of multiple peeling theory and its application to spider web anchorages. *Interface Focus* 5: 20140051. <http://dx.doi.org/10.1098/rsfs.2014.0051>

One contribution of 15 to a theme issue 'Biological adhesives: from biology to biomimetics'.

Subject Areas:

biomaterials, biomimetics, biomechanics

Keywords:

adhesion, numerical simulations, multiple peeling, spider web anchorages

Author for correspondence:

Nicola M. Pugno
e-mail: nicola.pugno@unitn.it

Numerical implementation of multiple peeling theory and its application to spider web anchorages

Lucas Brely¹, Federico Bosia¹ and Nicola M. Pugno^{2,3,4}

¹Department of Physics and 'Nanostructured Interfaces and Surfaces' Centre, Università di Torino, via P. Giuria 1, Torino 10125, Italy

²Laboratory of Bio-Inspired & Graphene Nanomechanics, Department of Civil, Environmental and Mechanical Engineering, Università di Trento, via Mesiano 77, Trento 38123, Italy

³Center for Materials and Microsystems, Fondazione Bruno Kessler, via Sommarive 18, Povo (Trento) 38123, Italy

⁴School of Engineering and Materials Science, Queen Mary University of London, Mile End Road, London E1 4NS, UK

FB, 0000-0002-2886-4519

Adhesion of spider web anchorages has been studied in recent years, including the specific functionalities achieved through different architectures. To better understand the delamination mechanisms of these and other biological or artificial fibrillar adhesives, and how their adhesion can be optimized, we develop a novel numerical model to simulate the multiple peeling of structures with arbitrary branching and adhesion angles, including complex architectures. The numerical model is based on a recently developed multiple peeling theory, which extends the energy-based single peeling theory of Kendall, and can be applied to arbitrarily complex structures. In particular, we numerically show that a multiple peeling problem can be treated as the superposition of single peeling configurations even for complex structures. Finally, we apply the developed numerical approach to study spider web anchorages, showing how their function is achieved through optimal geometrical configurations.

1. Introduction

Natural adhesives have captured considerable interest in recent years owing to their outstanding mechanical properties [1]. Well-known examples are gecko or insect adhesion [2,3], or spider web attachments [4], in which geometry, structure and material properties are essential in defining functionality. Gecko adhesion, which is based on van der Waals forces, achieves strengths of up to 1 MPa through the contact of billions of spatulae for each foot pad [5,6]. As in other cases of natural adhesives, the key to strong adhesion seems to lie in their hierarchical structure, which allows good adaptation to the surface and repeated contact splitting to increase the total peeling line without self-bunching [7,8]. The observation of these natural structures has inspired the design and realization of artificial dry adhesives (i.e. based on van der Waals forces) that guarantee simultaneous strong adhesion and smart, easy release, usually realized in polymers by means of 'mushroom-shaped' terminal elements tens of micrometres in size [9–13]. These structures, like gecko or insect terminal elements (spatulae), are tapered in shape [7], so that their detachment from the surface is reminiscent of the peeling of a tape from a substrate. Multiple peeling theory (MPT) [14] has recently been introduced by Pugno, and applied to cases of interest such as the delamination of a V-shaped elastic tape from a substrate, or to spider web anchorages [14,15].

The theory is a generalization of the well-known single peeling theory by Kendall [16] and predicts a critical value of the pull-off force corresponding to a limiting peeling angle which is reached as the delamination advances. Both the pull-off force and limiting angle only depend on the geometry of the tape, its elastic modulus and the interfacial energy. In [14], an assumption ('ansatz') is

formulated relating multiple to single peeling theory, as theoretically demonstrated for the symmetric double peeling case, stating that any multiple peeling problem can be treated as the superposition of single peeling ones, using Kendall's theory or its extensions. In this paper, we numerically implement this hypothesis.

The MPT is particularly useful to study the geometries of cases of interest found in Nature, where evolution has encouraged the optimization of structure and material properties for specific functions [17]. Spider web anchorages are one relevant case. For example, Sahni *et al.* [18] recently discussed the case of different attachment discs for cobweb-weaving spiders, showing that the attachment strengths of the different configurations ('scaffolding' and 'gumfoot' silk) are related to their specific function, namely locomotion and prey capture. In addition, Pugno *et al.* [19] compared MPT with atomistic modelling to demonstrate a synergy between material constitutive law and structural geometry, similarly to their previous findings on spider webs [20]. In this paper, we introduce a novel energy-based numerical model to address complex multiple peeling problems, including asymmetrical geometries or loading configurations. Results complement those obtained in previous studies and further clarify optimization mechanisms, analysing specific attachment disc configurations and adding further elements to interpret their particular structure.

The paper is structured as follows: in §2, the numerical model is outlined; in §3.1, the model is implemented by comparing its predictions with known MPT results and further simulations regarding a symmetric double peeling configuration are presented; in §3.2 and §3.3, results relative to asymmetrical double peeling geometries are discussed; finally, in §4, the results from previous sections are used to analyse two of the most common types of spider web anchorages and interpret their structure on the basis of their function.

2. Numerical model

We consider a model anchorage constituted by multiple tapes converging to a single point (or line), undergoing detachment by simultaneous or sequential peeling of the various tapes, and evaluate the adhesive properties of the system as a function of the specific configuration. To do this, we adopt a two-dimensional numerical-analytical model based on discrete nodal displacements: each tape is considered as a truss element of variable length, depending on the delaminated length, and each node has 2 degrees of freedom. As a first approximation, the material constitutive law is considered to be linear elastic and isotropic.

The simplest case is a V-shaped double peeling configuration, shown in figure 1, in which three nodes are necessary. An imposed displacement is incrementally applied on the structure vertex. For each increment, the balance between elastic energy and adhesive energy is computed between the deformed state and the delaminated state, assuming a discrete delamination length l_{del} . The external work term is absent as the simulation is in displacement control, so that, when delamination occurs, the position of the application of the force remains constant. Using the indices I, II and III for initial, deformed and delaminated states, respectively, delamination of the tapes $i = 1, 2$ takes place when the

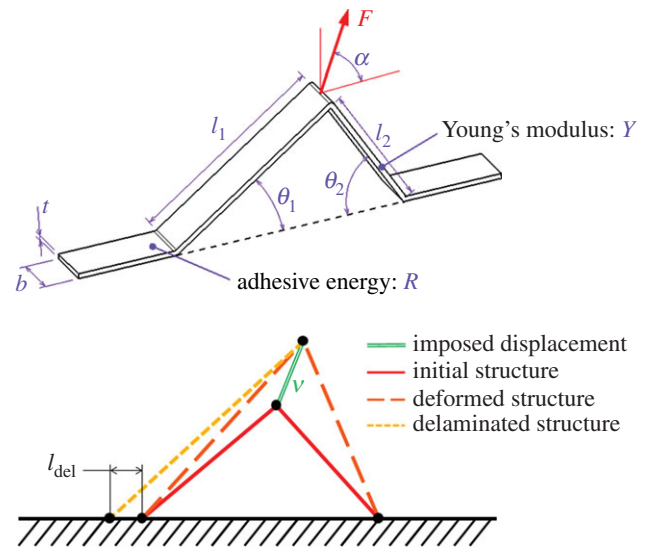


Figure 1. (a) Schematic geometry of an asymmetrical double peeling configuration. (b) Comparison between initial, deformed and delaminated configurations. For simplicity, delamination is shown on only one of the two branches.

stored elastic energy exceeds the energy needed to create a new area of surface $b \cdot l_{\text{del}}$ [14]

$$\frac{1}{2}YA \left[\frac{(l_{\text{II},i} - l_{i,i})^2}{l_{i,i}} - \frac{(l_{\text{III},i} - l_{i,i} - l_{\text{del}})^2}{l_{i,i} + l_{\text{del}}} \right] = bRl_{\text{del}}, \quad (2.1)$$

where Y is the tape Young's modulus, A is its cross section, b is its width, l is its length and R is the adhesive energy per unit area. Tape tensions (f_i), and, therefore, the total external load F corresponding to the imposed displacement, can be calculated from tape deformations Δl_i using Hooke's law

$$f_i = YA \frac{\Delta l_i}{l_i}. \quad (2.2)$$

The iterative process continues after delamination, considering the modified system configuration, i.e. attachment node displacements and tape length increments (as shown in figure 1).

3. Model results: double peeling

3.1. Symmetrical loading and symmetrical configuration

We first discuss a symmetrical peeling geometry with purely vertical loading (referring to figure 1: $l_1 = l_2 = l$, $\theta_1 = \theta_2 = \theta$, $\alpha = 90^\circ$). The chosen geometrical and mechanical properties of the tape are $t = 0.125$ mm, $b = 15$ mm, $Y = 3$ MPa and $l = 100$ mm. To begin with, we study the deformation of the structure only up to the onset of delamination. For different values of adhesive energy R , figure 2 shows the numerical predictions of the normalized force $F(\theta)/F(\pi/2)$ necessary to obtain delamination of the tapes as a function of the peeling angle θ (i.e. the angle of the deformed tape with respect to the surface at which delamination occurs).

These numerical results can be compared with analytical predictions using MPT [14], which in turn extends Kendall's single peeling theory [16]. Accordingly, the energy balance (as described in §2) for the peeling of a single tape is

$$\frac{f^2}{2btY} + f(1 - \cos(\theta)) - bR = 0. \quad (3.1)$$

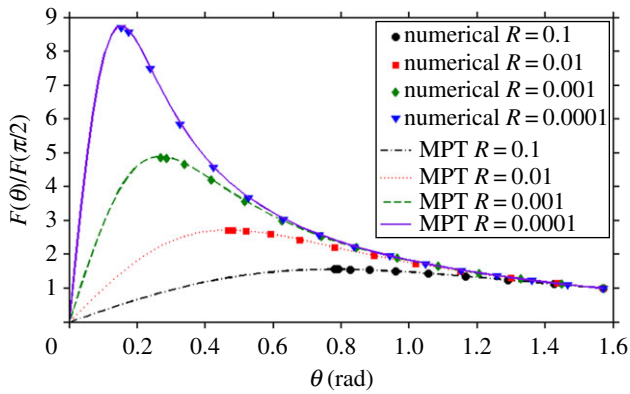


Figure 2. Analytically (MPT) and numerically calculated results for normalized delamination load $F(\theta)/F(\pi/2)$ versus peeling angle θ in a symmetrical double peeling configuration for various adhesive energies R (in J mm^{-2}).

The analytical expression for the single peeling force is, therefore,

$$f = btY \left[\cos(\theta) - 1 + \sqrt{(1 - \cos(\theta))^2 + \frac{2R}{tY}} \right]. \quad (3.2)$$

In this symmetrical case, it was demonstrated through energy balance considerations [14] that the total delamination force can also be obtained as the composition of two single peeling forces [16]

$$F = 2 \sin(\theta)f. \quad (3.3)$$

Analytical values using equations (3.2) and (3.3) are also plotted in figure 2 together with numerical predictions for different values, showing a perfect overlap. These results show that an optimal peeling angle is reached before delamination, in correspondence with which the peeling force is maximum, which depends on the adhesive energy of the tape–substrate and tape elasticity. Numerical solutions do not appear on the descending branch of the analytic curves for peeling angles smaller than this optimal angle. This is because, as we show below, optimal peeling angles (curve maxima) correspond to zero non-deformed (initial) angles, and thus smaller peeling angles would correspond to negative initial angles, which is physically meaningless [15].

Referring to figure 1, if deformation starts from an initial angle θ_0 , after deformation the strain in each of the two tapes is $\varepsilon = \Delta L/L = \cos \theta_0 / \cos(\theta) - 1$. Therefore, the tape tension can be expressed as

$$f = btY \left(\frac{\cos \theta_0}{\cos \theta} - 1 \right), \quad (3.4)$$

while the vertical external load at the vertex of the two tapes is expressed by equation (3.3). It is clear then that the optimal peeling force is obtained for $\theta_0 = 0$, as shown in figure 3a: the corresponding curve intersects the peeling force curve at its maximum value (the same mechanical properties as previously are used). We thus plot, in figure 3b, the external load F for $\theta_0 = 0$ as a function of the peeling angle θ as derived from equations (3.3) and (3.4), together with the peeling forces previously shown in figure 2 for various R values. The intersections between the curves, which correspond to the F values for which tapes with different R values delaminate, occur in all cases at the maximum of the peeling force curves, i.e. for optimal peeling angle values. This result confirms the fact that peeling cannot occur for the angle values below the

optimal angle, as the tape tension for these angles is smaller than that necessary to delaminate.

The optimal peeling angle is a function of the global deformability of the system, i.e. the deformation that the system can sustain before delamination occurs. This property can be quantified by the non-dimensional parameter $\lambda = 2R/(tY)$, representing the ratio between adhesion energy and elasticity [14]. We thus wish to derive the optimal peeling angle as a function of λ . To analytically obtain the value of the optimal peeling angle and force for a given λ value, given by the intersection of the curves in figure 3, we must equate equations (3.2) and (3.4). With simple algebraic manipulation, we obtain

$$2 \cos(\theta_{\text{opt}})^3 - (3 + \lambda) \cos(\theta_{\text{opt}})^2 + 1 = 0. \quad (3.5)$$

This equation can be solved for the non-dimensional parameter λ as a function of the optimal peeling angle θ_{opt} . Inverting the relation, we obtain the curve shown in figure 4 for θ_{opt} versus λ , showing a monotonically increasing nonlinear behaviour.

3.2. Asymmetrical loading and asymmetrical configuration

Next, we consider an asymmetric structure loaded asymmetrically, i.e. with a non-vertical load. As an example, the following parameters are chosen for the structure: $l_1 + l_2 = l = 100$ mm, $\theta_1 = 40^\circ$, $\theta_2 = 60^\circ$ (initial angles) and $R = 0.001 \text{ J mm}^{-2}$, while the tape's mechanical properties are the same as in the previous section. The parameter λ is of the order of 10^{-3} , so deformations at delamination are in this case very small. The delamination force calculated numerically as a function of the force application angle α is shown in figure 5 (only the first delamination is considered). Here, the range considered for α corresponds to the cases where both tapes are in tension. The observed behaviour can be explained by the fact that the two tapes no longer delaminate simultaneously: starting from small angles, tape 1 delaminates while tape 2 does not, and for large angles the opposite happens. In correspondence with the maximum of the curve, the symmetrical structure considered in the previous section is obtained.

To better understand these results, we can consider the case when tape deformations are negligible (i.e. the limit case of tapes with small λ). Considering the force equilibrium on the tips of the tapes with this hypothesis, from figure 1 we have

$$\begin{cases} F \cos(\alpha) - f_1 \cos(\theta_1) + f_2 \cos(\theta_2) = 0 \\ \text{and } F \sin(\alpha) - f_1 \sin(\theta_1) - f_2 \sin(\theta_2) = 0, \end{cases} \quad (3.6)$$

where f_1 and f_2 are the reaction forces from tapes 1 and 2, respectively. It is now possible to write the relation between the two tape tensions

$$f_1 \sin(\alpha - \theta_1) = f_2 \sin(\alpha + \theta_2). \quad (3.7)$$

Considering that only one of the tapes is delaminating, the corresponding delamination force is calculated using MPT. Using equation (3.7), it is possible to calculate the tension in the other tape, and using equation (3.6), the force applied to the system. Figure 5 shows that the simulation results (triangles) and the MPT solution (lines) coincide when the deformations are negligible.

The issue that remains to be clarified now is whether the calculation of multiple peeling forces from a superposition of

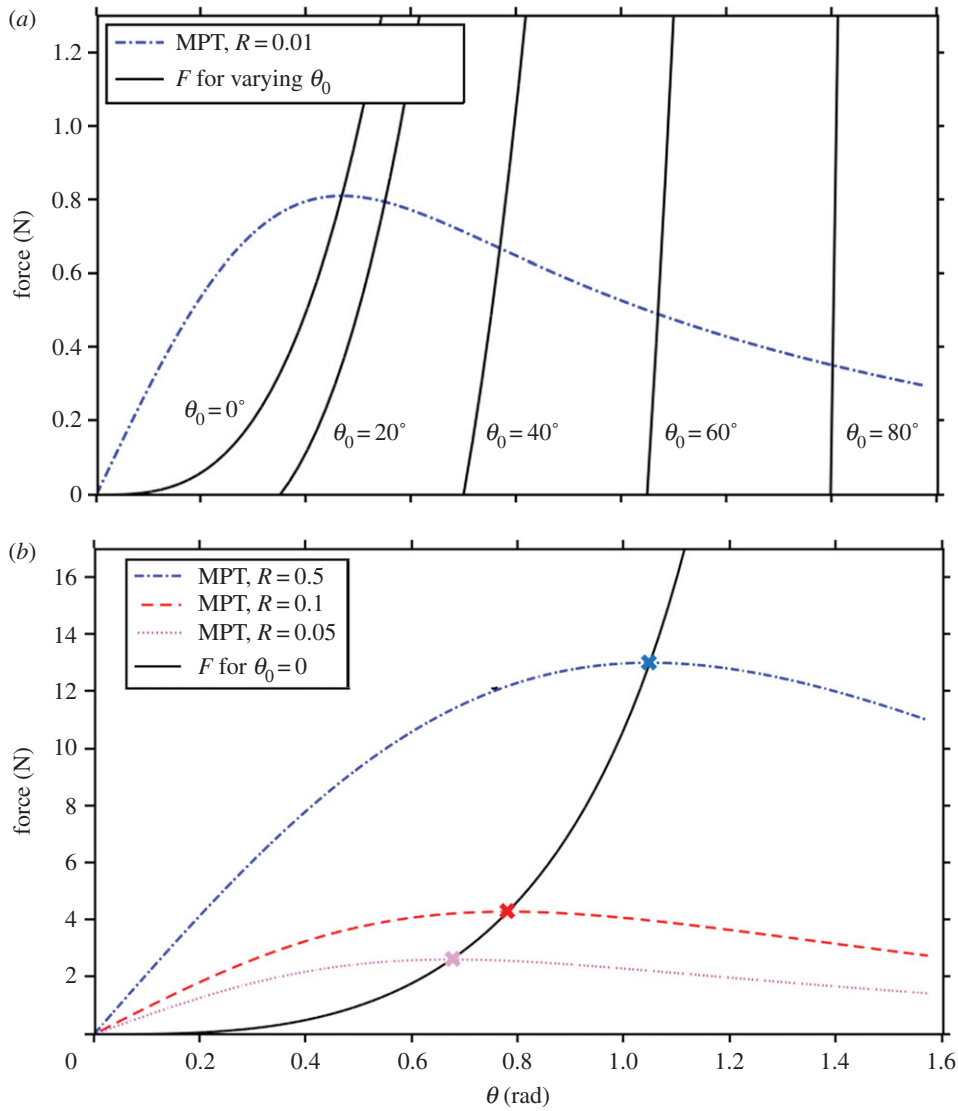


Figure 3. External applied force F and tape peeling forces versus peeling angle θ in symmetrical loading of a double peeling symmetric configuration: (a) $R = 0.01$, varying θ_0 ; (b) $\theta_0 = 0$, varying R . The intersection between curves occurs for $\theta_0 = 0$ at the maxima of the peeling force curves (indicated with crosses), i.e. for optimal peeling angle values.

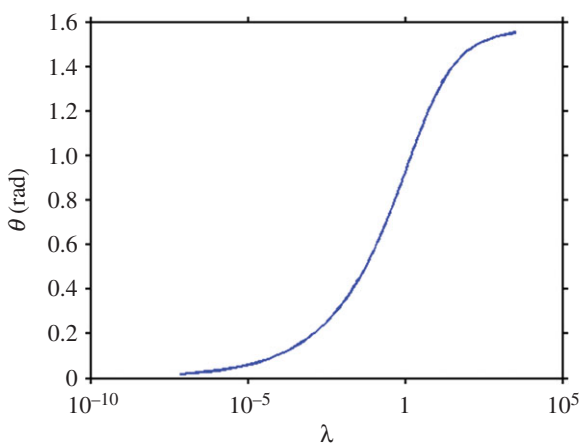


Figure 4. Optimal peeling angle $\theta = \theta_{\text{opt}}$ as a function of the non-dimensional parameter λ

Kendall single peeling forces remains valid in the case of moderate deformations of the system. To verify this, simulations are performed with $R = 0.1 \text{ J mm}^{-2}$, so that λ is of the order of magnitude of 10^{-1} . Mechanical properties, total tape length and tape sections are the same as reported

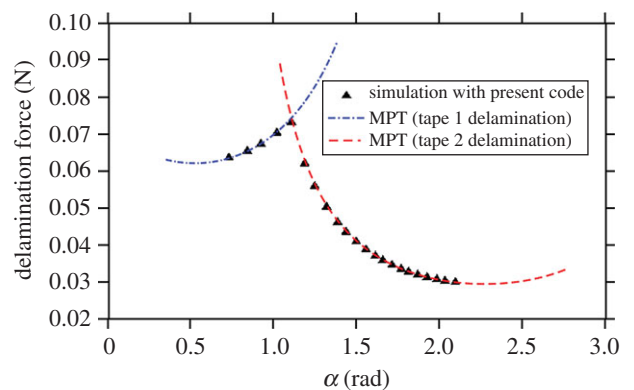


Figure 5. Delamination force versus applied force for a double peeling case for a quasi-rigid tape (small λ), calculated numerically (triangles) and by MPT (lines).

in the previous section. For various randomly chosen configurations, deformed angles and tensions in both tapes are numerically determined and compared with analytically calculated (using MPT) peeling forces. Table 1 shows typical results. The simulated peeling force of the delaminated tape can be obtained analytically if the deformed state (with

Table 1. Tape tensions and corresponding angles compared with peeling forces calculated using MPT. The values in bold/italics highlight the agreement between numerical and MPT-calculated values at delamination for the three systems considered as examples.

	system 1	system 2	system 3
α ($^\circ$)	75	100	60
θ_1 initial ($^\circ$)	40	40	45
θ_2 initial ($^\circ$)	60	60	45
θ_1 deformed ($^\circ$)	43.80	50.20	46.42
θ_2 deformed ($^\circ$)	76.44	63.60	65.84
tape 1 tension (N)	2.10	0.85	2.96
tape 2 tension (N)	1.71	2.15	0.80
external load (N)	3.21	2.62	3.33
MPT peeling force	3.10	2.76	2.96
tape 1 (N)			
MPT peeling force	1.71	2.15	2.06
tape 2 (N)			

corresponding angle modifications) is considered. For each considered configuration, and at each iterative simulation step, we find that the tension in the tape that delaminates is always coincident to the peeling force obtained by analytical single peeling theory considering the deformed system, thus confirming the hypothesis of MPT.

To better illustrate this, forces and deformations relative to system 1 in table 1 are illustrated schematically in figure 6. Here, delamination occurs for one of the tapes (on the right), and the tape tension is therefore equal to the peeling force calculated using the single peeling theory as demonstrated by MPT. In this state, the tension in the other tape is smaller than the peeling force, and delamination does not take place. The same happens for systems 2 and 3 in table 1, where delamination occurs for tapes 2 and 1, respectively.

3.3. Simulations of delamination evolution

We now consider the same structures considered previously, simulating the peeling phase beyond the first delamination, i.e. the entire detachment process. The same mechanical properties as in the previous sections are used, with $R = 0.01 \text{ J mm}^{-2}$. The structure is symmetric and the total tape length is $l = 20 \text{ mm}$ at the onset of the simulation. Figure 7a shows the force and the peeling angle as a function of the delamination length. Starting from $\theta = 90^\circ$, simulations show that the peeling force grows and tends to a limit value, and simultaneously the peeling angle decreases and also tends to a limit value. The structure becomes optimal for this peeling angle value, as the delamination force is maximal. The behaviour obtained simulating the entire process is equivalent to that obtained calculating single delaminations at various peeling angles. On the other hand, if we start from $\theta = 0$ (figure 7b), it can be seen that an abrupt slope change occurs for both force and peeling angle after the first delamination, after which both remain constant in the subsequent delamination phase, as the optimal force and angle have already been reached.

In the asymmetric case, we have verified that there is an optimal force direction at the tip of the tapes, depending on the geometry of the structure. If we now simulate the entire detachment process starting from the previous geometry,

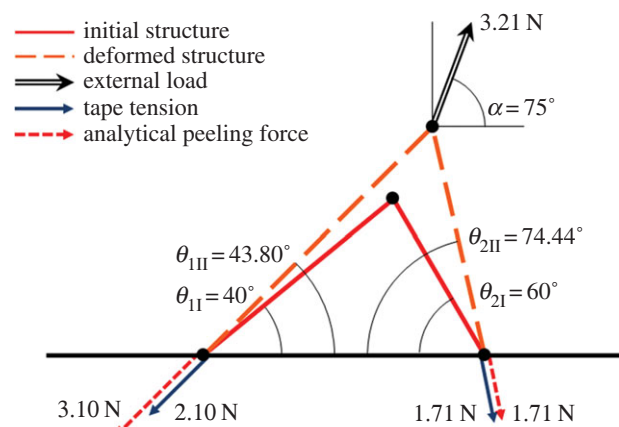


Figure 6. Graphical representation of system 1 in table 1, showing that numerically calculated peeling forces coincide with MPT-calculated ones where delamination occurs, if the deformed configuration is considered.

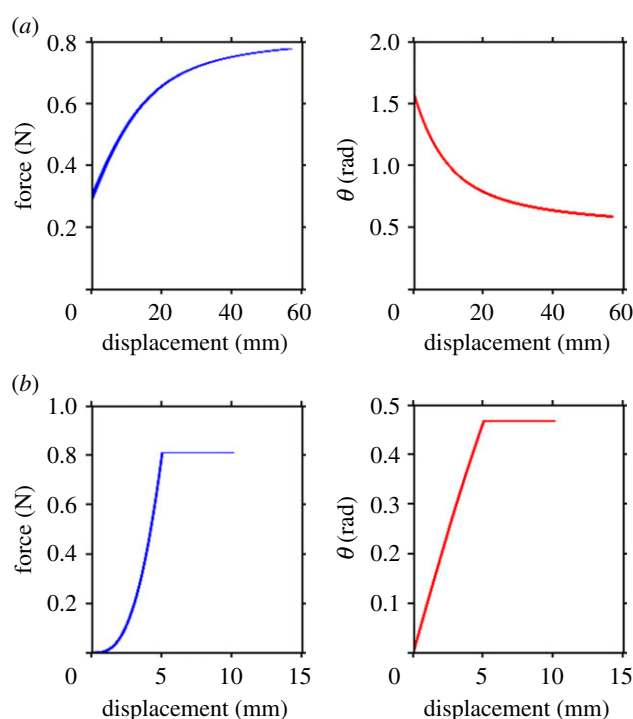


Figure 7. Symmetrical double peeling simulations. (a) Delamination force and peeling angle as a function of the delamination length starting from $\theta = 90^\circ$. (b) Delamination force and peeling angle as a function of the displacement starting from $\theta = 0^\circ$.

adopting a non-optimal force direction, the progressive delamination leads to a modification of the geometry in order to reach the equilibrium with both tapes under critical tension. Figure 8 shows the force as a function of the peeling angle for the two tapes. These curves are divided into two parts: the first (A–B) corresponds to a single-tape delamination phase necessary for the system to reach equilibrium, at which both tapes start delaminating together, and the second (B–C) to a phase in which the system reaches optimal angles.

All results in the previous sections are relative to two-dimensional geometries. However, this two-dimensional model is applicable to three-dimensional geometries in which the delamination force lies in a plane perpendicular to the surface. To extend the approach to more general three-dimensional cases, an additional angle would be necessary to describe the direction in space of the applied load, and in

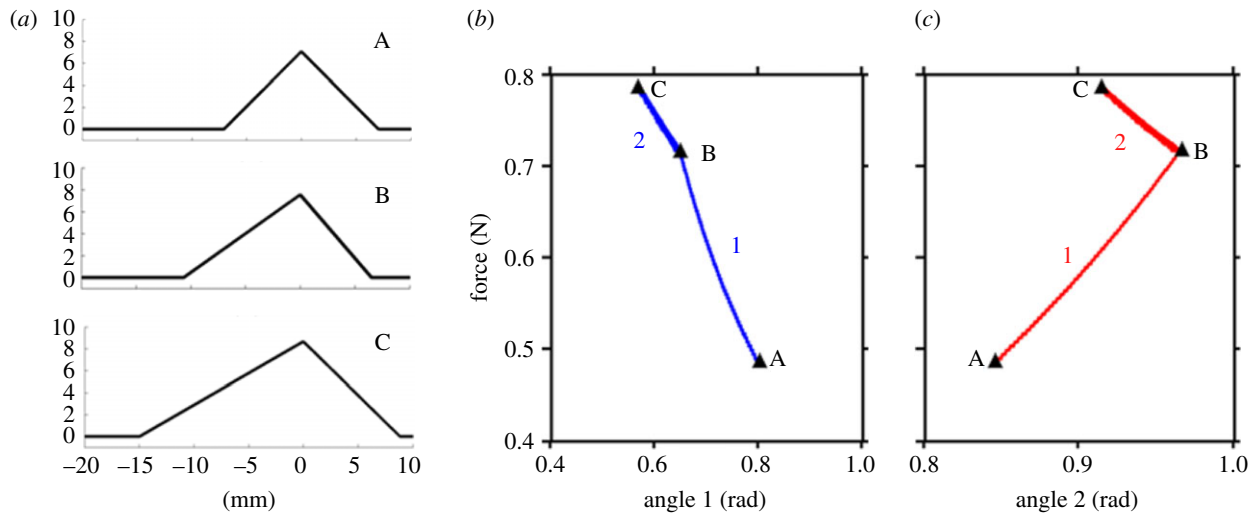


Figure 8. Delamination phases in a symmetrical double peeling simulation with a non-vertical force: (a) configuration at three successive time steps: A, B and C; (b) corresponding force versus peeling angle on the left tape; and (c) corresponding force versus peeling angle on the right tape. (Online version in colour.)

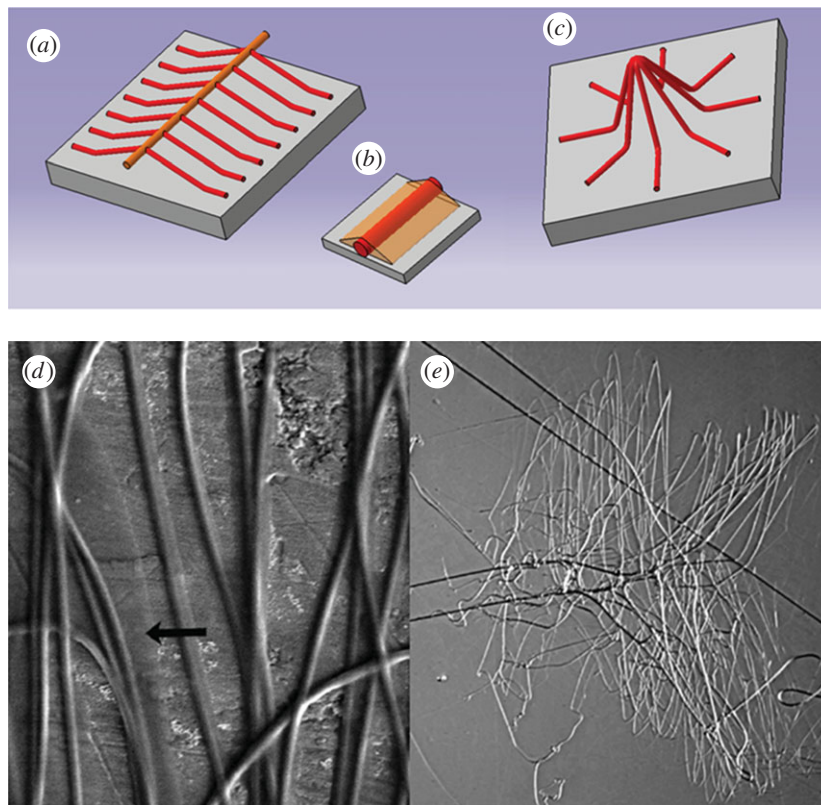


Figure 9. Spider silk attachment structures: (a) schematic of a 'staple-pin' architecture, (b) detail of a fluid-coated silk fibre, (c) schematic of a 'dendritic' architecture, (d) optical micrograph of spider web generic anchorage (adapted from [22]; copyright © 2009, the American Society for Biochemistry and Molecular Biology) also showing details of the fluid-coated silk fibre (indicated by an arrow) and (e) optical micrograph of a staple-pin anchorage. (Online version in colour.)

some cases a further angle describing the direction of the non-delaminated tapes with respect to delaminated ones (the two directions do not necessarily coincide). The problem can be treated, analytically and numerically, in a similar way to that illustrated above, and peeling force surfaces (instead of curves) can be obtained, e.g. as a function of the multiple angles mentioned above. Work is underway to study this problem, but the topic is beyond the scope of this paper.

4. Spider web anchorages

Spiders attach their silk draglines to substrates using so-called 'attachment discs' [4]. These structures involve pyriform silk

coated with a fluid that favours adhesion [21]. Recent studies have discussed the mechanics of different spider anchorages [18,20]: two main structures can be observed, with different functions. The first is a so-called 'staple-pin' structure ('scaffolding' silk; figure 9a), where branches are aligned and initially fully attached to the substrate, resulting in a plane morphology, which is used as a structural anchorage. Figure 9b shows a detail of a fluid-coated silk fibre: note the similarity with the adhesive tape considered in the previous section. The other possible architecture is a so-called 'dendritic' structure ('gumfoot' silk), which can be described as a radial branching structure where the pyriform silk fibres converge to a single point at a distance from the substrate,

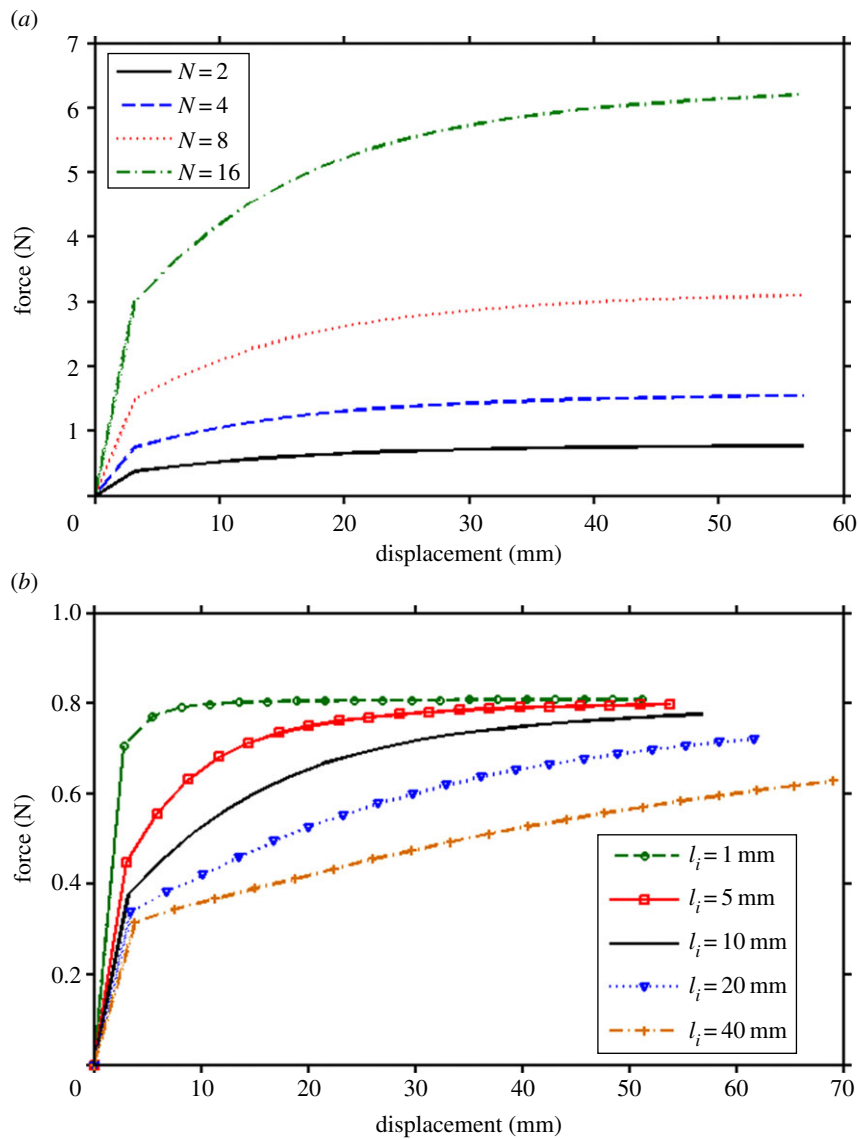


Figure 10. Force-displacement curves for a dendritic anchorage, for (a) varying number N of fibres in the anchorage ($l_i = 10$ mm) and (b) varying detached length l_i of the anchorage ($N = 2$).

resulting in a cone-like morphology (figure 9c) which is involved in spider prey capture. It has been shown [18,20] that, although they are based on the same pyriform silk, the two structures exhibit very different mechanical behaviour, which is functional to their role. To perform its function, the staple-pin anchorage must display high detachment strength, while the dendritic anchorage must exhibit a reduced pull-off force.

The first element that can explain the different pull-off forces observed for the two structures is the different extent of contact splitting occurring in the two morphologies. It is well known [7,8] that a larger number of contacts occurring in the pyriform silk implies a greater peeling line, and, therefore, a higher delamination strength. However, we will show in this section that other mechanisms related to the architecture of the anchorages can explain the differences between their different behaviour and maximal pull-off force.

The simulations reported here use the same mechanical properties as in the previous section, with an adhesive energy of $R = 0.01 \text{ J mm}^{-2}$. Since the approach is qualitative and only means to evaluate the role of geometry, results can be extended to any system with equivalent morphology and rigidity.

First, we will consider the dendritic anchorage. Owing to its conical symmetry, the relationship between force and displacement can be directly obtained from the symmetric double peeling configuration described in §3.1, modified by multiplying results by the appropriate number of tapes. As observed previously, in order to obtain a smaller delamination force, the initial tape angle must be close to $\theta = 90^\circ$. Figure 10a shows simulation results for various dendritic attachments with a varying number of tapes N , for the same initial tape angles ($\theta = 90^\circ$) and for a distance between substrate and the anchorage tip (i.e. detached tape length) of $l_i = 10$ mm. Clearly, the pull-off force is proportional to the number of contacts. The system is firstly deformed without delamination, with a linear force-displacement relationship (Hooke's law). Then, the tapes begin to delaminate and the peeling angle starts to vary, which results in an increase in the peeling force. This explains the elasto-plastic-like behaviour obtained in experimental [18] and numerical (figure 10) results. The peeling force saturates when the peeling angle is optimal. Exploiting this fact, it is clear that it is possible to maintain a small peeling force by increasing the initially detached tape lengths, since the displacement (and delamination length) necessary to reach the optimal configuration is greater. This is shown in figure 10b, where

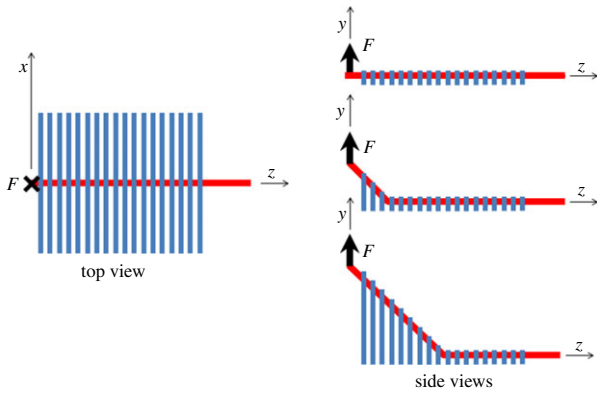


Figure 11. Schematic of the delamination mechanism in a staple-pin anchorage. (Online version in colour.)

force–displacement curves are compared for the same number of tapes but varying detached length. Thus, for a given delamination length, increasing the anchorage length (i.e. detached tape length) and using small initial angles are structural strategies that allow the pull-off force to be limited and ‘weak’ anchorages to be obtained. Notice from figure 10 how the choice of the specific type of attachment can lead to a consistent variation in the toughness of the structure (the area below the force–displacement curve), as well as in its strength.

The staple-pin anchorage, on the other hand, can be approximated by a succession of parallel symmetric double tapes (figure 11). The first observation regarding this system is that the displacement or force application point is adjacent to the substrate. Therefore, the initial angle of all double tapes is close to zero. This provides a configuration which requires a greater pull-off force than the dendritic system, as it is close to the optimal configuration, as explained in §3 (optimal deformed peeling angles correspond to zero initial angles). To simulate the anchorage during the delamination process, we assume that a displacement is imposed on the first double tape, and that the following double-tape displacement depends on the first one. Considering a quasi-rigid dragline, successive displacements linearly decrease with respect to the first one, as shown in figure 11 (side views).

If we indicate with dy_1 the displacement of the first double-tape tip, the successive displacements are given by

$$dy_j = dy_1 - Cz_j, \quad (4.1)$$

where dy_j are the imposed displacements of the j th double tapes, z_j are the positions of the j th double tapes along the z -axis in figure 11 and C is a constant that can be derived from equation (4.1) from the imposed displacements. In the simulation, each tape edge is coincident with the previous and the succeeding one, and tape centres are separated by $b = 15$ mm. The total number of double tapes in the system is $N = 6$, the initial tape length is 1 mm and the initial tape angle is 0. Figure 12 shows the delamination force as a function of the imposed displacement, with $C = 1/15$. It is apparent that the curve is the superposition of the delamination forces of the double tapes involved in the deformation of the system. Because C is relatively small, the first tape deforms and begins to delaminate; when it reaches a certain displacement value, the successive double tape begins to deform and delaminate, and so on. The reaction force is thus the sum of optimal peeling forces of the single delaminating tapes, which explains the step-like behaviour. The number of plateaus

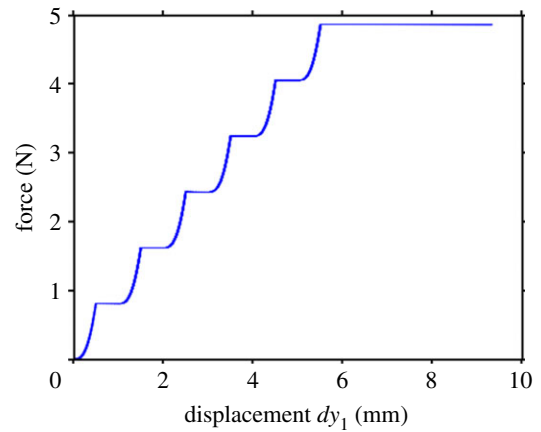


Figure 12. Force–extension curves for a staple-pin anchorage. (Online version in colour.)

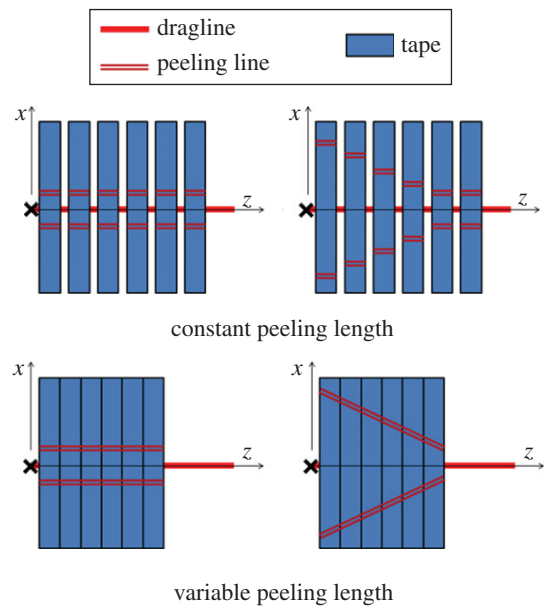


Figure 13. Mechanism for increasing the peeling length (and force) in a staple-pin anchorage: the peeling line increases its angle with respect to z as the delamination proceeds along z . (Online version in colour.)

in the curve is equal to the number of double tapes in the structure. When all six double tapes are delaminating, the force is maximal and remains constant.

A further example of a geometrical feature which contributes to the optimization of the adhesive strength of this type of anchorage can be observed by considering the high density of pyriform silk fibres in the staple-pin morphology (figure 9e), and the fact that the coating fluid contact area with the substrate is considerably larger than the dimension of the fibre (figure 9d). Thus, we can assume that the contact between the structure and the substrate is continuous in the z direction, i.e. there are no gaps between the contact areas of the different double tapes. The structure with gaps (above) and without (below) is shown schematically in figure 12. In the latter case, the peeling line is not parallel to the z direction, and is thus not equal for all detached tapes at a given delamination length of the dragline silk. The peeling length increases with the angle between the two peeling lines and the z axis, which in turn increases with the delaminated length of the dragline silk. Hence, the total peeling length and peeling force increase with the delamination length (figure 13).

Thus, we have shown that, using geometry only, the spider can tune and optimize the shape of the force–displacement curves of web anchorages, and thus generate different optimized constitutive laws for achieving specific functionalities (e.g. from stable/strong anchorages for attachment to instable/weak anchorages for capturing).

5. Conclusion

We have developed a new numerical approach to simulate the peeling behaviour of multiple fibrillar adhesives. We have implemented the model using MPT [14] for asymmetrical complex configurations. In particular, the model has been used to implement a previously postulated ‘ansatz’, namely that all multiple peeling problems can be solved as a superposition of Kendall single peeling configurations, provided they are applied to the appropriate deformed state of the system, as

stated by MPT and already analytically demonstrated for symmetric double peeling [14]. Finally, we have applied the new numerical model to study the specific adhesive properties of two distinct spider web anchorage types, showing how their structural features are instrumental in defining their constitutive law and overall adhesive strength and toughness, and, therefore, their effectiveness in accomplishing their function.

Acknowledgements. This work was carried out within the COST Action TD0906 on Biological Adhesives.

Funding statement. N.M.P. is supported by the European Research Council (ERC StG Ideas 2011 BIHSNAM no. 279985 on ‘Bio-inspired hierarchical super-nanomaterials’, ERC PoC 2013-1 REPLICA2 no. 619448 on ‘Large-area replication of biological anti-adhesive nanosurfaces’, ERC PoC 2013-2 KNOTOUGH no. 632277 on ‘Super-tough knotted fibres’), by the European Commission under the Graphene Flagship (WP10 ‘Nanocomposites’, no. 604391) and by the Provincia Autonoma di Trento (‘Graphene Nanocomposites’, no. S116/2012-242637 and reg. delib. no. 2266). L.B. and F.B. acknowledge support from BIHSNAM.

References

- Smith AM, Callow JA. 2006 *Biological adhesives*. Berlin, Germany: Springer.
- Autumn K, Peattie AM. 2002 Mechanisms of adhesion in geckos. *Integr. Comp. Biol.* **42**, 1081–1090. (doi:10.1093/icb/42.6.1081)
- Yao H, Gao H. 2006 Mechanics of robust and releasable adhesion in biology: bottom–up designed hierarchical structures of gecko. *J. Mech. Phys. Solids* **54**, 1120–1146. (doi:10.1016/j.jmps.2006.01.002)
- Sahni V, Blackledge TA, Dhinojwala A. 2011 A review on spider silk adhesion. *J. Adhesion* **87**, 595–614. (doi:10.1080/00218464.2011.583588)
- Arzt E, Gorb S, Spolenak R. 2003 From micro to nano contacts in biological attachment devices. *Proc. Natl Acad. Sci. USA* **100**, 10 603–10 606. (doi:10.1073/pnas.1534701100)
- Pugno NM, Lepore E. 2008 Living tokay geckos display adhesion times following Weibull statistics. *J. Adhesion* **84**, 949–962. (doi:10.1080/00218460802505374)
- Varenberg M, Pugno NM, Gorb SN. 2010 Spatulate structures in biological fibrillar adhesion. *Soft Matter* **6**, 3269–3272. (doi:10.1039/C003207g)
- Kamperman M, Kroner E, del Campo A, McMeeking RM, Arzt E. 2010 Functional adhesive surfaces with ‘gecko’ effect: the concept of contact splitting. *Adv. Eng. Mater.* **12**, 335–348. (doi:10.1002/adem.201000104)
- Geim AK, Dubonos SV, Grigorieva IV, Novoselov KS, Zhukov AA, Shapoval SY. 2003 Microfabricated adhesive mimicking gecko foot-hair. *Nat. Mater.* **2**, 461–463. (doi:10.1038/nmat917)
- Carbone G, Pierro E, Gorb SN. 2011 Origin of the superior adhesive performance of mushroom-shaped microstructured surfaces. *Soft Matter* **7**, 5545–5552. (doi:10.1039/C0SM01482F)
- Piccardo M, Chateauminis A, Fretigny C, Pugno NM, Sitti M. 2013 Contact compliance effects in the frictional response of bioinspired fibrillar adhesives. *J. R. Soc. Interface* **10**, 20130182. (doi:10.1098/rsif.2013.0182)
- Kovalev AE, Varenberg M, Gorb SN. 2012 Wet versus dry adhesion of biomimetic mushroom-shaped microstructures. *Soft Matter* **8**, 7560–7566. (doi:10.1039/C2SM25431J)
- Pugno NM. 2008 Spiderman gloves. *Nano Today* **3**, 35–41. (doi:10.1016/S1748-0132(08)70063-X)
- Pugno NM. 2011 The theory of multiple peeling. *Int. J. Fract.* **171**, 185–193. (doi:10.1007/s10704-011-9638-2)
- Afferrante L, Carbone G, Demelio G, Pugno N. 2013 Adhesion of elastic thin films: double peeling of tapes versus axisymmetric peeling of membranes. *Tribol. Lett.* **52**, 439–447. (doi:10.1007/s11249-013-0227-6)
- Kendall K. 1975 Thin-film peeling—the elastic term. *J. Phys. D* **8**, 1449. (doi:10.1088/0022-3727/8/13/005)
- Gorb SN. 2008 Biological attachment devices: exploring nature’s diversity for biomimetics. *Phil. Trans. R. Soc. A* **366**, 1557–1574. (doi:10.1098/rsta.2007.2172)
- Sahni V, Harris J, Blackledge TA, Dhinojwala A. 2012 Cobweb-weaving spiders produce different attachment discs for locomotion and prey capture. *Nat. Commun.* **3**, 1106. (doi:10.1038/ncomms2099)
- Pugno NM, Cranford SW, Buehler MJ. 2013 Synergetic material and structure optimization yields robust spider web anchorages. *Small* **9**, 2747–2756. (doi:10.1002/smll.201201343)
- Cranford SW, Tarakanova A, Pugno NM, Buehler MJ. 2012 Nonlinear material behaviour of spider silk yields robust webs. *Nature* **482**, 72–76. (doi:10.1038/nature10739)
- Sahni V, Blackledge TA, Dhinojwala A. 2010 Viscoelastic solids explain spider web stickiness. *Nat. Commun.* **1**, 19. (doi:10.1038/ncomms1019)
- Blasingame E et al. 2009 Pyriform spidroin 1, a novel member of the silk gene family that anchors dragline silk fibers in attachment discs of the black widow spider, *Latrodectus hesperus*. *J. Biol. Chem.* **284**, 29 097–29 108. (doi:10.1074/jbc.M109.021378)